Engineering 29 (2023) 120–129

Contents lists available at ScienceDirect

Engineering

journal homepage: www.elsevier.com/locate/eng

Research
Material Science and Engineering—Article

The Nanoscale Density Gradient as a Structural Stabilizer for Glass Formation

Shaoxiong Zhou [a,b,*], Bangshao Dong [b,c], Yanguo Wang [d], Jingyu Qin [e], Weihua Wang [d,*]

[a] China Iron and Steel Research Institute Group, Beijing 100081, China
[b] Institute of Advanced Materials, North China Electric Power University, Beijing 102206, China
[c] Jiangsu JITRI Advanced Energy and Materials Research Institute, Changzhou 213032, China
[d] Beijing National Laboratory of Condensed Matter Physics, Institute of Physics, Chinese Academy of Sciences, Beijing 100190, China
[e] Key Laboratory for Liquid–Solid Structural Evolution and Processing of Materials (Ministry of Education), Shandong University, Jinan 250061, China

ARTICLE INFO

Article history:
Received 17 October 2022
Revised 29 November 2022
Accepted 10 January 2023
Available online 29 March 2023

Keywords:
Rapid cooling
Amorphous solid
Density gradient
Electron tomography
Atomic clusters

ABSTRACT

The rapid cooling of a metallic liquid (ML) results in short-range order (SRO) among the atomic arrangements and a disordered structure in the resulting metallic glass (MG). These phenomena cause various possible features in the microscopic structure of the MG, presenting a puzzle about the nature of the MGs' microscopic structure beyond SRO. In this study, the nanoscale density gradient (NDG) originating from a sequential arrangement of clusters with different atomic packing densities (APDs), representing the medium-range structural heterogeneity in $Zr_{60}Cu_{30}Al_{10}$ MG, was characterized using electron tomography (ET) combined with image simulations based on structure modeling. The coarse polyhedrons with distinct facets identified in the three-dimensional images coincide with icosahedron-like clusters and represent the spatial positions of clusters with high APDs. Rearrangements of the different clusters according to descending APD order in the glass-forming process are responsible for the NDG that stabilizes both the supercooled ML and the amorphous states and acts as a hidden rule in the transition from ML to MG.

1. Introduction

Different manufacturing routes can produce the same material with different internal structures that grant the material markedly different properties and practical applications [1,2]. An intrinsic structural feature of metallic glasses (MGs) made by the rapid quenching of metallic liquids (MLs) is the short-range order (SRO) of the atomic arrangement, which can result in various possible characteristics in terms of the microscopic structure and heterogeneity [3]. SRO structures [4–10] have been intensively investigated via a series of theories, as well as through simulations using a much higher cooling rate than the actual rate used in MG manufacturing. Although the structural evolution from ML to MG, such as the coarsening of atomic clusters, is greatly depressed in the simulated model structures, various structural models such as the hard sphere disordered dense packing [11], cluster dense packing [12], free volume [13], and shear transformation zone [14] models have been put forward to help in understanding the amorphous structure. One important feature of SRO structures in MGs is the formation of different atomic clusters with various polyhedron configurations. These atomic clusters, whose existence has been confirmed by Hirata et al. [15] using a sub-Ångstrom electron beam diffraction technique, construct a framework for the amorphous structure and strongly dominate the local characteristic structures responsible for the heterogeneous nature of MGs at the sub-nanometer scale. Because of the MGs' isotropic properties, according to correspondence between structure and properties, MGs can be thought of as macroscopically homogeneous materials. But the characteristics of the microscopic structure in MGs are highly localized at the sub-nanometer or single-atomic-cluster scale. Differences in the atomic arrangements from place to place result in a microscopic structure with a randomly heterogeneous nature.

In an MG, the structural heterogeneity that inherently stems from the ML is closely related to the glass-forming process. Because the dynamics of the atomic rearrangements govern the critical transition process from an ML to an MG [16–18], the

* Corresponding authors.
E-mail addresses: sxzhou@atmcn.com (S. Zhou), whw@iphy.ac.cn (W. Wang).

https://doi.org/10.1016/j.eng.2023.01.010

fluctuating atomic arrangements in the ML have an important effect on the structural heterogeneity of the MG [19,20]. The spatial heterogeneity in the dynamics of fluctuating atomic arrangements as a function of temperature during the process from a supercooled ML to an MG has been directly visualized by means of electron correlation microscopy with a sub-nanometer resolution [21]. Moreover, both experimental and simulation studies have confirmed that structural heterogeneities are locally favorable for forming close-packed icosahedron-like clusters in three-dimensional (3D) space, greatly slowing the dynamics of the ML and promoting the glass-forming ability [18,19].

Many experimental investigations on structural heterogeneity have been intensively conducted by means of high-resolution transmission electron microscopy (HRTEM), extended X-ray absorption fine structure spectroscopy, neutron diffraction, synchrotron X-ray nano-computed tomography (nano-CT), atomic probe tomography, and dynamic atomic force microscopy [22–28]. Aside from SRO, the presence of medium-range order and even long-range topological order in MGs has been demonstrated [3,29,30]. Spatial density variation, fractal order, and their characteristics, which are closely related to heterogeneity in the microscopic structure, have also been revealed in MGs. Huang et al. [26] reported 3D density fluctuations and fractal order in MGs by means of nano-CT and interpreted these results based on the evolution of low-density regions during the glass formation and deformation processes. A fractal structure and a homogeneous structure with an atomic-level crossover length have been respectively proposed by Lei et al. [22] and Pekin et al. [23], based on the results of *in situ* X-ray diffraction, tomography, and molecular dynamics (MD) simulations. Mechanical heterogeneities at the nanoscale and no a fractal atomic-level structure with the packing of all atoms or solute-centered clusters in MGs have been explored by several research groups based on HRTEM, dynamic atomic force microscopy observations, and MD simulation results [31,32]. However, although HRTEM has a resolution at the atomic level, the two-dimensional (2D) HRTEM images of MGs comprising one element or multiple components all show quite similar characteristics, and detailed information on the MGs' real microscopic structures cannot be directly inferred from the features present in HRTEM images. Thus, it is difficult for the different local microscopic structures in MGs to be visualized experimentally using HRTEM.

Electron tomography (ET) is a quantitative 3D imaging technique that requires no symmetry or order and can be used to reconstruct the interior structure of an object from its serial projections. Recently, Yang et al. [33] developed an experimental method to directly determine all the 3D atomic positions in an MG using atomic ET combined with advanced iterative algorithms. Some single atomic clusters derived from the resolved atomic positions coincide with simulated polyhedral configurations. Although many atomic clusters can be resolved by means of atomic ET, almost no detailed information on the structural evolution that results in coarse clusters and on the characteristics of the structural stabilizer in the transition from an ML to an MG has been disclosed thus far. Therefore, further experimental evidence is still needed on medium-range structural heterogeneity and locally characteristic microscopic structures in MGs, such as coarse clusters and 3D heterogeneous density distribution. In this study, the nanoscale density gradient (NDG), as a representation of the medium-range microscopic structure in as-prepared $Zr_{60}Cu_{30}Al_{10}$ MG, was identified by means of ET. An NDG originates from rearrangements of atomic clusters with different atomic packing densities (APDs) during the transition from an ML to an MG; it represents the microscopic structure at the nanometer level and can act as a structural stabilizer in the glass-forming process. The NDG also bridges the structural gap between the SRO and long-range disordering in MGs. In this work, the formation of an NDG is interpreted and discussed based on sequential rearrangements of clusters with different APDs in a supercooled ML.

2. Materials and methods

2.1. Selection and preparation of the amorphous ribbon sample

In addition to poor ductility [34], zirconium–copper-based amorphous alloys have high strength and high hardness; thus, they have wide-ranging applications as bulk MGs in mobile phone hinges, brackets, card-taking needles, car door lock buckles, and sports goods. Because this study on the disordered structure of amorphous solids could only be carried out based on a comparison of transmission electron microscope (TEM) observation, theoretical simulation of the model structure, and HRTEM images calculated using the model structure, the qualified MG samples used in this study were required to have the combined advantages of a good glass-forming ability, a stable amorphous structure suitable for the preparation of TEM samples and TEM observation, and atoms with available potential functions as needed for structural modeling using a large-scale MD simulation. A ZrCuAl MG system aligning with the above selection criteria was selected and synthesized using melt spun procedures. Individual zirconium (Zr), copper (Cu), and aluminum (Al) metals with respective purities of 99.6%, 99.99%, and 99.9% were mixed according to the composition of $Zr_{60}Cu_{30}Al_{10}$ in an alumina crucible and heated to 1200 °C for 2 h in a high-frequency induction furnace. Under an argon (Ar) atmosphere, the ML was injected through a narrow nozzle onto the surface of a fast-rotating copper wheel and rapidly quenched into a long amorphous metallic ribbon with a thickness of about 26 μm and a width of about 5 mm.

2.2. TEM sample preparation

The ribbon specimens for HRTEM characterization were prepared as follows. First, a disc with a diameter of 3 mm was cut from the as-prepared ribbon with a thickness of approximately 26 μm using an ultrasonic disc cutter (Model 601, Gatan, Inc., USA). Then, the thickness of the center area of the disc was reduced to about 15 μm using a mechanical dimple grinder (Model 656, Gatan, Inc.). The thickness at the center area of the dimpled sample, which was kept at −20 °C at the cold specimen stage, was thinned to electron transparency by means of argon ion milling (Model 691, Gatan, Inc.). Glancing angles of 4° and 2° were respectively set for the incident Ar-ion beam at the initial and later stages of the milling process in order to reduce the thickness as much as possible. Finally, a very low-energy ion beam emitted from an ion gun operated at an accelerating voltage of 150 V was positioned incident to the surface plane of the TEM sample at a glancing angle of 1° in order to remove the amorphous surface layer that may have been slightly relaxed by the ion beam during the early and later stages of the ion milling process.

2.3. Tomographic tilt and 3D reconstruction

A set of HRTEM tomographic tilt series was acquired from the $Zr_{60}Cu_{30}Al_{10}$ sample using a TEM (Tecnai G2, Thermo Fisher Scientific, USA) equipped with precision tilt stages and supported by sophisticated image-processing resources. Bright field images were collected while operating the TEM at 200 kV. The tilt series with tilt angles ranging from −71° to 66° in steps of 1° consisted of a total of 128 images, as shown in Fig. S1 in Appendix A. These 128 experimental images were sufficient to produce a good 3D reconstruction. To monitor any potential damage induced by the electron beam, we took 0° images before, during, and after the

acquisition of each tilt series and ensured that no noticeable structural changes were observed in the selected areas.

A large-volume reconstruction of the $Zr_{60}Cu_{30}Al_{10}$ from the aligned experimental tilt series of the HRTEM images was made using Icosprocess algorithms [35]. The tomographic reconstruction was accomplished by means of the weighted simultaneous iterative reconstruction technique using multiple iterations. The number of iterations was determined by visually inspecting the spatial resolution and noise of the reconstruction for an optimal balance. A final 3D reconstructed image was obtained after refinement of the initially reconstructed 3D image.

2.4. Determination of TEM sample thickness

The thickness of the prepared TEM sample with a thickness of H and width of W was examined via the tilting method. A cross-correlation between the projected width $L(\alpha)$ of the selected area in the sample and the real width and thickness of the same position in the sample is shown in Fig. S2 in Appendix A. The tilt angle α follows this equation:

$$L(\alpha) = W \cdot \cos\alpha + H \cdot \sin\alpha \quad (1)$$

As shown in Figs. S3(a)–(d) in Appendix A, the projected widths of the selected area were measured at two different tilt angles. Using the projected widths measured at two different tilt angles, as shown in Figs. S3(b) and (d), the real thickness of H was determined to be about 6 nm by solving the two combined equations for the two tilt angles.

2.5. Model structure construction

To construct the model structure, a large-scale atomic/molecular massively parallel simulator was used to carry out MD simulations for a $Zr_{60}Cu_{30}Al_{10}$ ML consisting of 10 000 atoms [36]. A dense atomic packing configuration with the dimensions of 5.8 nm × 5.8 nm × 5.8 nm, which coincided with the measured thickness of the solid amorphous alloy (Fig. S3), was produced based on Newtonian mechanics, employing embedded atom method potentials [37]. The equilibrium ML at the high temperature of 2000 K was quenched to 300 K (6.56 $g{\cdot}cm^{-3}$) at an MD cooling rate of 10^{12} $K{\cdot}s^{-1}$ with zero external pressure and was then completely relaxed at 300 K. The full coordinates of every atom residing inside the amorphous alloy were determined, and an inherently inhomogeneous structure with atoms in a variety of different local configurations was presented by this model structure.

2.6. HRTEM image simulation

HRTEM image simulation based on the computer-constructed model structure of the $Zr_{60}Cu_{30}Al_{10}$ MG was performed using the xHREM program package. The atom positions and model size used as the lattice parameters of the unit cell based on the MD calculations were input for simulations of the HRTEM images by performing dynamic electron diffraction calculations using the multi-slice method [38]. The parameters used in the simulation were as follows: a spherical aberration coefficient of 0.5 mm, beam convergence of 0.003 nm^{-1}, aperture radius of 5 nm^{-1}, and sample thickness of 6 nm.

2.7. Searching for distinct polyhedrons and their connections

Distinct polyhedrons and their connections were searched for in the modeled structure, which is divided into many cubic cells centered by each atom. Each line connecting the center atom and one of the neighboring atoms is bisected by a plane perpendicular to this line. All the inner planes enclose the cell, in which the enclosed part of the space is closer to the center atom than to any other atoms. The nearest neighbors to the center atom are the atoms sharing a common cell surface. For multicomponent elements, the bisection can be weighted by the atomic size. Faces of the enclosed cell with an area below 0.25% of the total area are discounted. The arrangement and geometry of the nearest neighboring atoms around the center atom are described by a four-number Voronoi index $<n_3, n_4, n_5, n_6>$ whose components respectively represent the number of triangles, quadrangles, pentagons, and hexagons of a Voronoi polyhedron [39]. The pentagon content for an icosahedron-like polyhedron is defined by $n_5/(n_3+n_4+n_5+n_6)$. Connection scenarios of Voronoi polyhedrons were assessed for the center atoms of those polyhedrons that were nearest neighbors or second nearest neighbors.

3. Results

3.1. The NDG represents the microscopic structure

Based on the tomographic tilt series of the 2D HRTEM images (shown in Fig. S1), 3D images were reconstructed. Fig. 1(a) shows a general view of the disordered structure. To clearly reveal the microscopic features, an enlarged image corresponding to the area marked by a black box in Fig. 1(a) is shown in Fig. 1(b), where independent polyhedrons with different sizes ranging from about 0.5 to 2.0 nm and various configurations are randomly distributed. A polyhedron with a diameter of approximately 0.5 nm is roughly coincident to the size of a single icosahedron constructed by a central atom surrounded by the atoms in the same single shell. The isolated atoms and single atomic clusters in the ML must join together to form a complex network in the MG during rapid solidification. As extra atoms join a single atomic cluster or as additional single atomic clusters merge together during the solidification of the ML, the size of the newly formed atomic clusters in the MG must inevitably increase. The polyhedrons in Fig. 1(b) that are clearly larger than 0.5 nm correspond to aggregations of atomic clusters. Regardless of whether the clusters are formed via the joining of extra atoms or the merging of individual atomic clusters (or both), the newly formed atomic clusters have many different structures with various configurations. In general, depending on the number of merged individual clusters, the configurations of the newly formed atomic clusters change, resulting in merged clusters with very rich surface configurations. Consequently, the presence of complex morphology among the atomic clusters in MGs can be predicted.

Through careful inspection of the configurations of these polyhedrons in Fig. 1(b), even though their morphologies appear to be very complex, it was found that most have a roughly similar morphology, such as a nearly rounded shape. In addition, there are some large polyhedrons with irregular shapes, such as a curved band-like configuration. To reveal the features of the image intensities of the different polyhedrons, a stereo display of Fig. 1(b) is shown in Fig. 1(c), which was obtained using the image intensity as the third vertical axis perpendicular to the image plane. The differences in the image intensities of every polyhedron in Fig. 1(b) are clearly revealed by the stereo profiles. It can easily be seen from the stereo display that the image intensity is high at the central part of the polyhedrons and low at the rim areas, resulting in a heterogeneous image intensity for these polyhedrons. In addition to the heterogeneity of the image intensities, Fig. 1(c) shows another feature: Spatial intensity gradients form for every image intensity peak and the neighboring intensity valleys around this peak. The polyhedrons with different sizes, image intensities, and configurations in the 3D image are obviously different from place to place, leading to spatial heterogeneity in the microscopic struc-

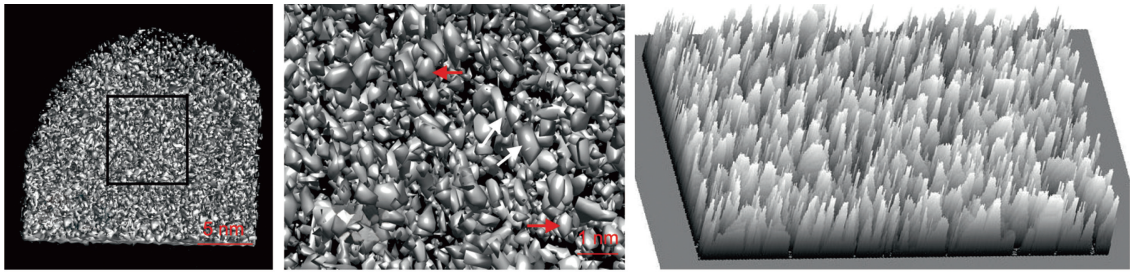

Fig. 1. Reconstructed 3D images. (a) 3D image at low magnification showing a general view of the disordered structure. (b) Enlarged image of the area indicated by the black box in part (a); red and white arrows indicate the roughly rounded and curved band-like polyhedrons, respectively. (c) Corresponding stereo display of part (b).

ture of the MG. Although the atomic arrangements of these polyhedrons are closely correlated to the SRO, the microscopic structure represented by these polyhedrons is completely disordered.

The intensity distribution in the 3D image results from the contribution of all the component Fourier vectors, which were created by the serial tilt 2D TEM images and used to reconstruct the 3D image. The correlated component Fourier vectors all contribute to the image intensity at the same position in the reconstructed 3D image. When more correlated component Fourier vectors contribute to the image intensity at the same position, the corresponding intensity at this position in the 3D image increases. Because the correlated component vectors in the Fourier space stem from the correlated image intensity peaks in the differently oriented 2D HRTEM images, among all the serial tilt 2D HRTEM images, only the image intensity peaks produced by the same atomic cluster or aggregation of clusters in the MG can result in correlated component vectors in the Fourier space. If the image intensity peaks present in more 2D HRTEM images are produced by the same atomic cluster or aggregation of clusters, there will be more correlated component vectors in the Fourier space and a stronger image intensity in the 3D image, corresponding to this atomic cluster or aggregation of atomic clusters.

To establish a correlation between the distribution of the image intensity and the spatial atomic arrangement in $Zr_{60}Cu_{30}Al_{10}$ MG, a computer-generated model structure with the dimension coincident to the measured thickness of the real TEM sample (as shown in Fig. S3) was made and is shown in Fig. 2(a). It should be pointed out that the computer modeling of MGs has intrinsic limitations due to the large disparity between the actual cooling rate used in experiments to quench an ML to manufacture the MG and the ultrafast cooling rate used in the MD simulation—that is, the cooling rate in computer modeling is about six orders faster than that in experimental manufacturing, which results in the real MG having a much more evolved structure and lower potential energy than the computer-generated MG. Although there are obvious differences between the microscopic structures of real and computer-generated MGs, simulation of the 2D HRTEM images based on the computer-generated model structure can reveal the imaging characteristics of the disordered structure of the MG to some extent.

2D HRTEM images along the different orientations were calculated using serial defocus values at steps of 5 nm. Fig. 2(b) shows one of the simulated HRTEM images along the [100] direction, in which the image intensity peaks and valleys are all distributed randomly. Some adjacent image intensity peaks are not clearly separated from each other, forming a mountain-range-like configuration. To reveal intensity variations in the simulated HRTEM image, a stereo display of Fig. 2(b) was constructed in the same way as Fig. 1(c) and is shown in Fig. 2(c). In this stereo display, the image intensity profiles are clearly exhibited in 3D space. The intensity gradually decreases from each individual peak to the neighboring valleys. In addition to the intensity difference between the peak and valley positions, strong and weak intensities can be identified among the different peak positions. Similarly, different intensities are present among the different valley positions.

To correlate the image intensity and spatial atomic arrangement, narrow atomic columns with a small cross-section that were respectively compatible with the areas of individual intensity peaks and valleys were extracted along different directions at the positions corresponding to the individual peaks and valleys in the model structure. Figs. 2(d) and (e) show two typical atomic columns extracted along the [100] direction at the peak and valley positions, respectively. The obvious difference between these atomic columns is the spatial atomic density at the peak position, which is always higher than that at the neighboring valley position. Therefore, the governing factor for the creation of the intensity peaks and valleys in the simulated HRTEM images is the spatial APD in the atomic columns along the projected direction. Based on the established correlation between the spatial APD and the intensities in the simulated 2D TEM image, it is known that only the spatial atomic segments in the MG with high APDs are responsible for high image intensities in the 2D HRTEM image, and they have a greater chance to produce high image intensity in other HRTEM images along different orientations than atomic segments with low APDs. Thus, every HRTEM image in a tomography series reflects the characteristics of the spatial APD along the different orientations. High image intensity in 2D HRTEM images creates visible intensity in the Fourier space and contributes to the component vectors. However, low image intensity in 2D HRTEM images creates nearly invisible intensity in the Fourier space and contributes to the background.

The polyhedrons in the 3D image were reconstructed by the component Fourier vectors originating from the visible intensity in the tomographic serial 2D HRTEM images and are highly correlated with the densely close-packed atomic segments in the MG. Therefore, the difference in the image intensity of the polyhedrons in Fig. 1 is responsible for the spatial heterogeneity in the arrangement of the densely close-packed atomic segments. Based on the correlation between the intensity distribution in the 3D image and the spatial APDs of the atomic arrangements, more atoms are accumulated along the direction through the central part than through the rim portion of the polyhedrons. As a result, regardless of the direction, the image intensity is high at the central part of the polyhedrons and low at the rim of the same polyhedrons, unless the light is intentionally projected by the display software along a specific direction in the 3D image in order to specially exhibit the ultrafine surface features on the polyhedron.

The image intensity gradient in the 3D images shown in Fig. 1 is the spatial nanoscale APD gradient or NDG, which is an important representation of the microscopic structure in an MG. The NDG created by the aggregation of icosahedral clusters with high ADP

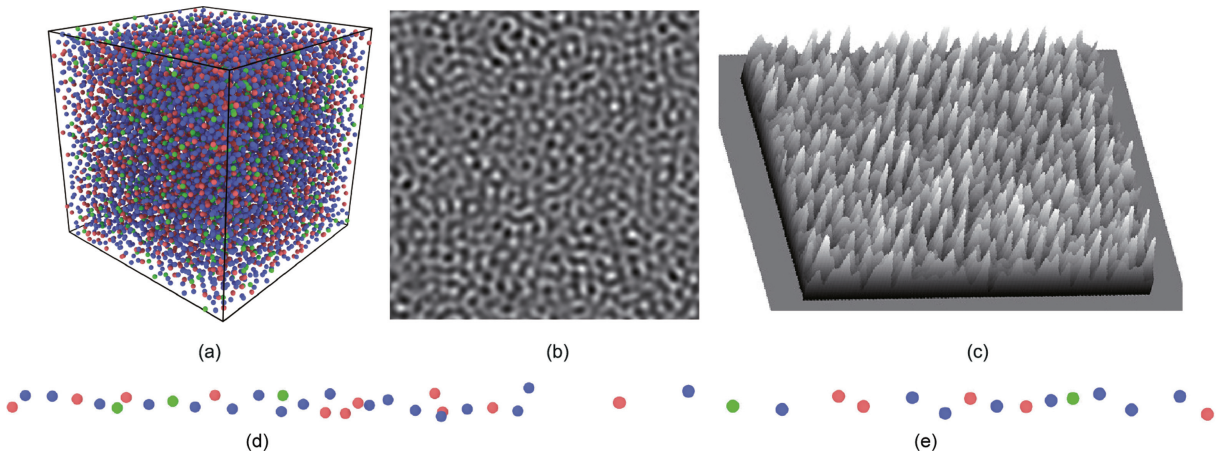

Fig. 2. Imaging characteristics of an amorphous solid. (a) A computer-generated model structure of a $Zr_{60}Cu_{30}Al_{10}$ amorphous solid with dimensions of 5.8 nm × 5.8 nm × 5.8 nm was made at 300 K; the blue, red, and green balls respectively represent the Zr, Cu, and Al atoms. The dense packing of the 10^4 atoms is inherently inhomogeneous because of atoms in various local configurations. (b) The calculated 2D HRTEM image along the [100] direction and (c) the corresponding stereo display show a randomly heterogeneous image intensity. (d, e) Atomic columns with a normal cross-section respectively compatible with the areas of (d) the image intensity peaks and (e) the valleys in part (b) were extracted at the corresponding positions in the model structure shown in part (a) along the [100] direction. The APD at the peak position is obviously higher than that at the valley position.

and non-icosahedral clusters with low APD was searched for in the model structure shown in Fig. 2(a) and is shown in Fig. 3(a). In this NDG, the icosahedral clusters made by the atoms connected by lines show a high atomic density with respect to the nearby non-icosahedral clusters. As shown in Figs. 3(b) and (c), since the atomic potential energy and the volume clearly decreased during the quenching process, while the contents of some icosahedron-like clusters simultaneously continuously increased with the decrease of the melt temperature, the microscopic structure in both the ML and MG was strongly dominated by an NDG constructed by a spatially mixed arrangement of icosahedral clusters with high ADP and non-icosahedral clusters with low ADP. Because vitrification clearly involves some selection of lower energy configurations in a supercooled ML, the spatial NDG, as a typical characteristic structure, must be the predominant cluster configuration of efficient atomic packing that is energetically favorable for the structural stability of both the supercooled ML and the glassy states [40]. It should be emphasized that the NDG is an isolated stable structure in an MG and can be thought of as the basic structural unit in constructing an MG or glass nuclei over the critical size in nature. As an independent and stable structural unit, an NDG is formed by different clusters that are rearranged according to descending APD order; it is clearly different from the reported heterogeneities at both the microscale and macroscale in MGs, because these heterogeneities mainly refer to differences in the average composition and/or structural features between different areas in MLs.

Because both the NDG and the SRO can respectively describe the distinct characteristics of the microscopic structure of an MG at different spatial scales, there may be some intercorrelation between them. However, their fundamental difference is that the SRO only shows correlations of the nearest neighboring atoms, whereas the NDG characterizes the correlations of atoms far beyond the nearest neighboring atoms. In other words, the NDG factually represents the correlations of the atoms beyond the short range. Thus, the NDG characterizes the microscopic structure at a medium-range scale and can bridge the structural gap between the SRO and long-range disordering in an MG. It should also be noted that the NDG and SRO are sufficiently distinct such that the behavior of the NDG cannot be readily predicted from the SRO alone, particularly in a supercooled ML, even though both are closely connected with the atomic arrangement and are interrelated to some extent.

3.2. Surface reconstruction of coarse clusters and/or the NDG

All atoms in the shell of a cluster are commonly arranged in a regular manner that closely relates to the APDs, resulting in facets

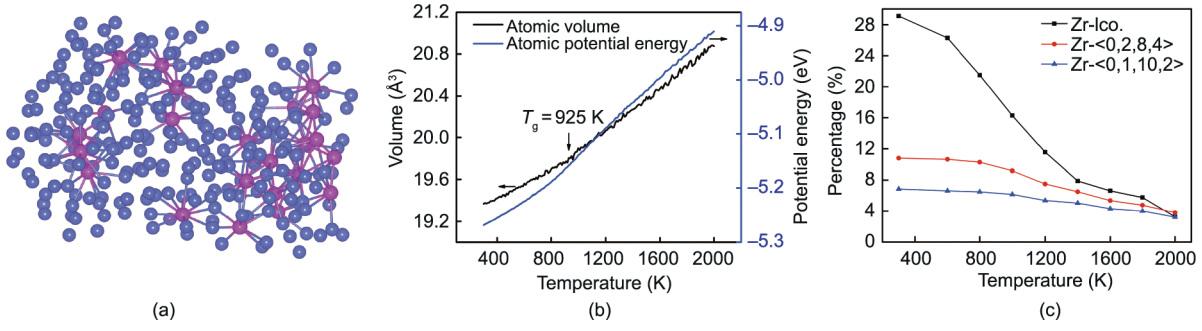

Fig. 3. Microscopic structure of the NDG. (a) Aggregation of icosahedral clusters with high APD and non-icosahedral clusters with low APD leads to the formation of an NDG in $Zr_{60}Cu_{30}Al_{10}$ MG; the magenta balls represent the center atoms of the icosahedral clusters, while the other atoms are indicated by blue balls for simplicity. A difference in atomic densities can be seen between the outlined icosahedral clusters and the nearby non-icosahedral clusters. (b) Characteristic variation of the atomic potential energy and volume vs temperature, obtained from structure modeling, where T_g represents the glass transition temperature. (c) Calculated relation between the content of some icosahedron-like clusters and temperature, where Zr-Ico refers to the total Zr-centered icosahedron, and Zr-<0,2,8,4> and Zr-<0,1,10,2> are the top two Zr-centered icosahedron-like clusters in $Zr_{60}Cu_{30}Al_{10}$ alloy.

with different configurations in the shells of the clusters. The surface enclosed by these facets over the whole shell forms a polyhedron with the distinct 3D geometrical configurations described by the famous Voronoi polyhedrons [39]. Among the various Voronoi polyhedrons, icosahedrons with a total of 12 pentagonal vertices and icosahedron-like clusters with triangles, quadrangles, and pentagonal and hexagonal vertices made by tetrahedrons are advantageous for the most efficient atomic filling of space and are responsible for high APDs. A common characteristic of these densely close-packed clusters is that the geometries of their atomic arrangements and their facets at the full or local surface are coincident with five-fold symmetry or pentagons, which has been theoretically predicted and experimentally detected in MLs and MGs [12,15,18,19].

Although rapid cooling causes an ML to solidify very quickly, a structural evolution accompanied by coarsening of the clusters inevitably occurs in this process. This extensive structural evolution also leads to obvious coarsening of the clusters; furthermore, the coarsened clusters eventually undergo surface reconstruction during the transition from the ML to an MG. Usually, the surface reconstruction of the coarsened clusters means that the coarse clusters in the MG receive a limited inheritance of atomic structure and surface morphology from the original clusters in the ML. Even though clusters with the typical features of icosahedron or icosahedron-like polyhedrons are likely to remain in the MG, the configuration of the remaining clusters in the MG may be distorted from the original polyhedrons in the ML to some extent. As a result, the icosahedral clusters in the MG retrograde to five-fold symmetry-rich and/or pentagon-rich polyhedrons. Thus far, individual atoms at the surface of the polyhedron cannot be seen due to the limited resolution of the ET technique. Therefore, the detailed atomic arrangements at the surface of the clusters were explored in the 3D image. The facets at the surface of the polyhedrons could be recognized directly in the 3D image, and facets with distinct sizes and features could be clearly identified. These facets and their arrangements were used to search for five-fold symmetry-rich and/or pentagon-rich polyhedrons in the 3D images. As shown in Fig. 4(a), five facets with a triangle shape and unequal sizes were found around two neighboring vertices of a polyhedron with a size greater than 1 nm, allowing local five-fold symmetrical and/or pentagonal geometries to be identified on the polyhedron. This cluster is obviously larger than the perfect icosahedron, and the total surface configuration is significantly different from that of a perfect icosahedron.

Because the MG is composed of multiple elements, when the shell of a single icosahedron or icosahedron-like polyhedron is constructed of different atoms, the sizes of the surface facets are no longer identical to each other, and the corresponding surface morphologies deviate from the prototypical ideal configuration to some extent. The presence of five-fold symmetry-rich and/or pentagon-rich polyhedrons was confirmed by searching for the coordination number of the densely close-packed atoms residing in the computer-generated model structure shown in Fig. 2(a). Fig. 4(b) displays some icosahedron-like clusters that were searched for among the defined five-fold symmetrical vertex content. It is worth noting that the population of the icosahedron-like clusters searched for in the model structure directly depends on the five-fold symmetrical vertex content selected for the search. Variation in the selected five-fold symmetrical vertex content resulted in a change in the population of the searched-for icosahedron-like clusters in the model structure. Therefore, the total population of the searched-for icosahedron-like clusters with different five-fold symmetrical vertex contents were found to be dominant in the model structure.

The spatial distribution of some icosahedron-like clusters was extracted from Fig. 4(b) and is shown in Fig. 4(c). Fig. 4(d) shows one enlarged icosahedron-like cluster isolated from Fig. 4(b). Although this cluster is not coarsened enough with respect to the polyhedron shown in Fig. 4(a), the five-fold symmetrical vertices surrounded by five facets are clearly exhibited; thus, polyhedrons with high APDs in the 3D image can be predicted to correspond to the icosahedron-like clusters in the MG. In Fig. 4(d), a facet constructed by the same kinds of atoms in the shell has the shape of an equilateral triangle, whereas a facet constructed by two different kinds of atoms in the shell has the shape of an isosceles triangle, which is distinctly different from an equilateral triangle. Therefore, the facets shown in Fig. 4(d) are not identical to each other. The five-fold symmetrical vertices formed by these non-identical triangle facets also deviate from the prototypical ideal five-fold symmetrical vertices made by identical atoms in the same shell.

In addition to the polyhedron with triangular surface facets and the local five-fold symmetrical and/or pentagonal geometries, a different kind of surface reconstruction was found. As shown in Fig. 5(a), an isolated polyhedron with a near sphere-like configuration was explored, and almost no obvious facet could be found on its surface. The minimal total surface energy principally dominates the surface reconstruction of the clusters in the coarsening process. Because the total surface energy can be simply expressed as a product of the total surface area and the energy per unit area at the surface, the total surface area and energy per unit area are two important factors relevant to the total surface energy of the atomic clusters. A sphere-like surface can effectively reduce the total

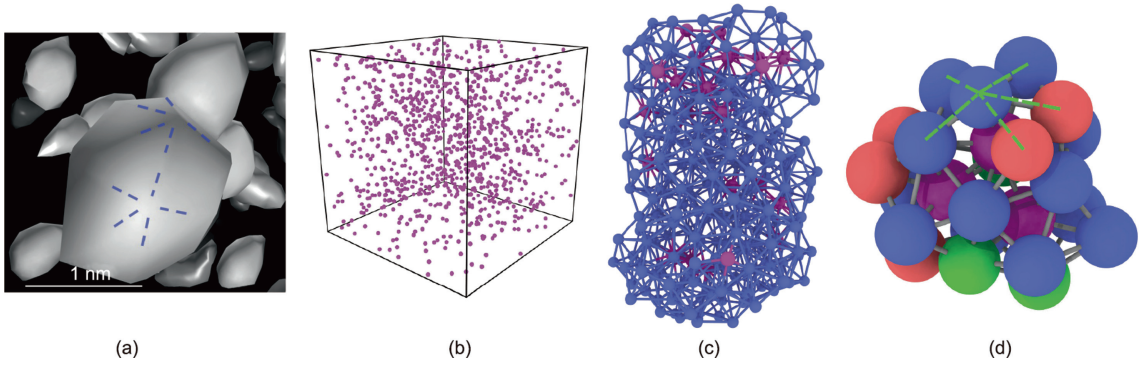

Fig. 4. Distinct characteristics of the coarse clusters. (a) An isolated coarse polyhedron with regularly distributed surface facets and local pentagonal vertices marked by dashed blue lines was traced in the 3D image. (b) Icosahedron-like polyhedrons with a pentagonal vertex content of 0.75 and over were searched for in the computer-generated model structure; for simplification, every magenta ball represents one icosahedron-like polyhedron. (c) A segment of the atomic arrangement extracted from part (b) shows the spatial distribution of some icosahedron-like polyhedrons, where the magenta balls represent the center atoms of icosahedron-like polyhedrons and the other balls represent the surrounding atoms. (d) An enlarged individual polyhedron with the local pentagonal vertex indicated by dashed green lines; the magenta balls indicate the Zr atoms at the center of the individual polyhedron, while the balls with other colors have the same meanings as in Fig. 2(a).

surface area, whereas surface facets significantly reduce the energy per unit area. Therefore, surface reconstruction is always accompanied by a balancing of these two factors for lowering the total surface energy of the atomic clusters during the coarsening of the clusters. When the minimal total surface area is more favorable than the minimal energy per unit area for lowering the total surface energy of the coarse clusters, the surface reconstruction is dominated by the minimal total surface area. Usually, facets are a disadvantage for the minimal total surface area; in this case, whether or not facets are present on the surface directly depends on their effects on the minimal total surface energy. If the facets are advantageous only for lowering the local surface energy and not for maintaining the minimal total surface energy, there may be facets at the corresponding local surface but no facets appearing on other surfaces or the whole surface. However, facets may be present on the whole surface when they are favorable for lowering both the local surface energy and the total surface energy or for maintaining the minimal total surface energy. On other hand, if the minimal energy per unit area is more advantageous than the minimal total surface area for lowering the total surface energy, then facets coincident to the planes with the minimal energy per unit area appear at the surface, as shown in Fig. 5(b). Consequently, surface reconstruction can cause the surface morphology of the coarse clusters to change from configurations with the minimal total surface area to configurations with full facets with the minimal energy per unit area at any time, as the size of the coarse clusters varies during the process of structural evolution. It should also be pointed out that the facets can have a different energy per unit area if the atoms are arranged in different ways in the facet planes. Thus, changes between different facets may reduce the total surface energy of the atomic clusters and, in the coarsening process of the clusters, it may also be possible for different facets to change frequently on the outside surface of the clusters in order to maintain the minimal total surface energy as the cluster's size increases. In other words, the surface morphologies of the coarse clusters are size-dependent to some extent; as a result, the coarse clusters have various possible surface morphologies, such as the polyhedrons shown in the 3D images.

In the supercooled ML, the icosahedrons have a strong tendency to both aggregate and spatially correlate with other icosahedrons or icosahedron-like polyhedrons. Self-aggregated and interconnected icosahedral clusters are very common in ZrCu alloy systems [41], causing the resultant polyhedrons to exhibit expanded sizes and reconstructed surface configurations. The widely scattered distribution of the icosahedron-like clusters in the simulated model structure matches well with the randomly distributed polyhedrons observed in the 3D image, although the clusters have different sizes. Because the content of icosahedron-like polyhedrons is dominant in some Zr-based MGs and the corresponding MLs [15,42], it can be concluded that the icosahedron-like polyhedrons surrounded by other non-icosahedral polyhedrons are responsible for the formation of the NDG detected in the 3D image. The cluster environment formed by the NDG is favorable for efficient atomic filling of the space and for stability in the transition from the ML to the MG.

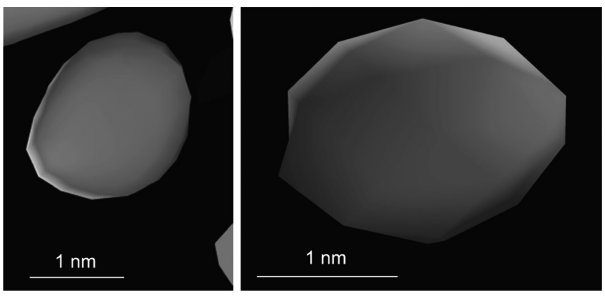

Fig. 5. Other characteristics of the coarse clusters. The individual coarse polyhedrons isolated from the 3D image show (a) nearly no facets and (b) some irregularly arranged facets at their surfaces.

3.3. Local reconstruction relevant to the connection of coarse clusters with high APDs

When the dynamic and instantaneous clusters in the ML become part of a static solid structure, the cluster arrangements undergo a substantial change during the cooling of the ML. In addition to isolated coarse clusters, connections between dominant coarse clusters can occur during the transition from the supercooled ML to the MG. The evolution of these polyhedron connections can result in correlations being developed between dominant coarse clusters beyond the nearest-neighbor atoms at the sub-nanometer scale and extending to the first-neighbor and second-neighbor polyhedral motifs at the nanometer scale and/or medium range. Depending on the different connection schemes, the connected coarse clusters can have various geometrical configurations. Usually, these different connection schemes are simultaneously present in the MG. As shown in Fig. 6(a), some coarse clusters with high APDs are obviously cross-linked in different ways that can be classified into two categories: coarse clusters connected via a neck with different sizes and coarse clusters connected with no neck at the connection area.

Because the atomic arrangement and structure can change from one cluster to another cluster through the connection area, it is clear that—regardless of whether or not necks appear—connections between coarse clusters with high APDs have indeed resulted in the local reconstruction of both the atomic arrangement or structure and the surface at the connection areas. Usually, the atomic arrangements of two different clusters are related at the connection areas; thus, the atomic arrangements at the connection areas are transitional in nature, causing the atomic arrangements at these areas to totally change or deviate from those of the connected clusters to some extent.

These different connection scenarios between the icosahedron-like polyhedrons were explored by tracing the coordination number of the densely packed atoms in the modeling structure shown in Fig. 2(a), although the evolution of the structure and the coarsening of atomic clusters are greatly reduced in this model structure. The obtained results are shown in Figs. 6(b)–(f). Based on these results, different joining features between the coarse clusters were identified. The various features of the joined clusters were isolated from Fig. 6(b) and are exhibited in Figs. 6(c)–(f). During the transition from the ML to the MG, the cooperative rearrangement of atoms was clearly involved in the connectivity of the dominant coarse clusters. Different cooperative rearranging regions of the atoms were present at the joint area, leading to different characteristic connections between these clusters. If the rearranged atom regions at the contact area were large enough to match with the clusters, a neck did not appear at the contact area. As shown in Fig. 6(c), the overlapping polyhedrons seemed to construct a new polyhedron with a larger size. A neck appeared when the atomic rearrangement regions at the contact area were small or narrow with respect to the coarse clusters. Figs. 6(d)–(f) show three different features of the necks. As the neck becomes narrow, the type of connection changes gradually from face-like (Fig. 6(d)) to edge-like (Fig. 6(e)) and finally to the vertex-like (Fig. 6(f)) form. Based on a careful inspection of the atomic arrangement at the connection areas shown in Figs. 6(c)–(f), the atomic arrangements of the clusters are changed via the atoms shared by the connected clusters; for example, as shown in Fig. 6(e), the atomic arrangement changes from the triangle or pentagonal shape of the cluster to a square

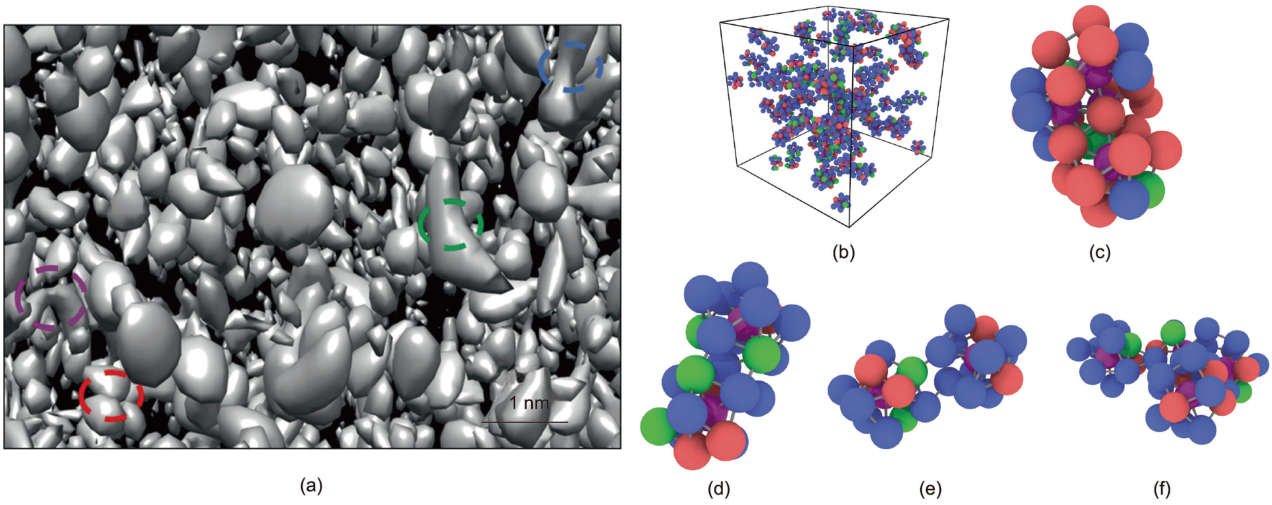

Fig. 6. Characteristics of the aggregated clusters. (a) Reconstructed 3D image showing two different types of interconnection between polyhedrons with high APDs; the green circle indicates an interconnection of clusters without a neck, while the blue, purple, and red circles indicate interconnections with necks of different sizes. (b) Different connection configurations between the Zr-centered icosahedral clusters identified in the computer-generated model structure; purple balls represent the central atoms of the individual clusters, while other balls with different colors have the same meanings as in Fig. 2(a). (c–f) Enlarged structural models of different types of connection: (c) an interconnection of clusters without a neck, which is responsible for an interpenetration joining; and (d, e) necks at the sub-nanometer level and (f) necks at the atomic level respectively correspond to face-like, edge-like, and vertex-like links of clusters.

shape at the connection area. The arrangement of the neighboring atoms that connect the different clusters is clearly different from the atomic arrangements of the connected clusters and is responsible for local reconstruction of the atomic arrangement; as a result, the surface alternation occurs at the connection areas. Depending on the different situations of structural evolution in the supercooled ML and during the glass-forming process, local reconstruction at the connection areas may occur simultaneously with the formation of coarse clusters or after the coarsening of the clusters.

It should be noted that the correlation of the nearest neighboring atoms in two connected icosahedrons remains unchanged from one icosahedron to another icosahedron if they are connected by sharing one common atom. However, aside from this commonly shared atom, the other atoms around the commonly shared atom in one icosahedron and the neighboring atoms in the other icosahedron at the connection area are obviously farther away than the nearest neighboring atoms. Thus, the correlations between these second and/or farther neighboring atoms across the different icosahedrons are entirely different from the neighboring correlations of second and/or farther neighboring atoms in any one of the two connected icosahedrons. If two coarse clusters with different types of atomic packing are connected, regardless of the connection scenarios between them, the correlation of the neighboring atoms across the two clusters is changed via the commonly shared atom (or atoms). These different characteristic necks are revealed in the 3D image shown in Fig. 6(a), where the connection of the clusters changes from a face-like or edge-like scenario to a vertex-like configuration as the size of the neck is reduced from the sub-nanoscale to the atomic level. Because of the strong tendency of icosahedral polyhedrons in a supercooled ML to self-aggregate and interconnect [41], icosahedral polyhedrons connected to each other and to other icosahedron-like polyhedrons may result in dense packing of the icosahedral polyhedrons in MGs. Therefore, the connectivity of polyhedrons with high APDs can effectively increase the size fluctuation of the NDG in both the supercooled ML and the MG.

4. Discussion

The glass formation of supercooled MLs is a result of the dynamic arrest that originates from the environment-dependent energetics of local clusters [43]. The energies of local clusters in MLs or MGs can be very different from those of isolated clusters. Thus, a material's glass-forming ability does not depend only on the dense atomic packing of the icosahedrons or icosahedron-like polyhedrons themselves [19,20]; the local cluster environment around the icosahedral clusters can also greatly affect the slowing dynamics and glass formation of a supercooled ML [18–20,29,30,32]. The NDG formed by densely close-packed icosahedrons or icosahedron-like clusters promotes a dense structure and high viscosity of the supercooled ML, leading to promotion of the material's glass-forming ability. Kinetically, the loose structures in an ML can result in a low viscosity and thus make atomic rearrangement relatively easy, which is also favorable for crystallization. Because icosahedral clusters or aggregations of icosahedral clusters with slow mobility can also reduce the mobility of neighboring non-icosahedral clusters [41], the local cluster structure relevant to the NDG also significantly slows the dynamics and/or dynamic arrest in a supercooled ML. Moreover, in addition to elongating their own lifetimes, icosahedral clusters or aggregations of icosahedral clusters can increase the lifetimes of all their neighboring cluster types [41]. Because the stability of the local structure in an ML depends on the lifetimes of all the involved clusters, the lifetime elongation caused by neighboring icosahedral clusters results in a general increase in the stability of the liquid state, particularly when an NDG forms in a supercooled ML—a stability increase that will become more pronounced as the temperature decreases to the glass-forming temperature. In addition to their longer lifetime, icosahedral clusters have slower mobility and lower energy than other non-icosahedral clusters in an ML. These different properties cause icosahedral and non-icosahedral clusters to exhibit different effects on the dynamic slowdown of an ML and result in spatial heterogeneity in the dynamics of the icosahedral and non-icosahedral clusters. Once the NDG relevant to the icosahedral and icosahedron-like clusters forms in the supercooled ML, as a local dominant structure, it is the key to the dynamic slowdown and dynamic arrest of the local structures in the ML during the glass-forming process. The strong dynamic slowdown effect of the NDG and of the icosahedral and icosahedron-like clusters is enhanced as the temperature decreases, so this spatial heterogeneity in the dynamics is obviously temperature dependent [21]. As the temperature decreases

to the glass-forming temperature, the effect of the dynamic arrest resulting from the NDG made by the icosahedral and icosahedron-like clusters drives the local structures into nonergodicity, which prevents the supercooled ML from relaxing to thermodynamic equilibrium and impedes crystallization processes during the course toward the glassy transition. When the temperature of the ML cools to the onset temperature of glass formation, triggering the transition from the ML to an MG, the NDG in the supercooled ML ultimately results in the formation of the MG in the whole alloy system, and the microscopic structure of the MG is eventually dominated by the NDG at the medium-range level. The route of microstructure development from an ML to an MG is schematically illustrated in Fig. 7.

In addition to the case of $Zr_{60}Cu_{30}Al_{10}$ MG, icosahedron and icosahedron-like clusters are the dominant clusters in many reported modeling structures of ZrCu and ZrCuAl ML systems [19,44]. Similar to the icosahedron and icosahedron-like clusters in this study, the population of the clusters in such systems increases with a decrease in the ML temperature. Parallel studies show that icosahedron and icosahedron-like clusters with a high APD and common behavior in both undercooled and supercooled MLs promote both higher stability of the liquid state and better inheritance of the structural heterogeneity profile during cooling. Because the trends of icosahedron and icosahedron-like clusters in ZrCu and ZrCuAl MG systems are quite similar to that in $Zr_{60}Cu_{30}Al_{10}$ MG, it is reasonable to believe that the NDG model in the present study is also applicable to other ZrCu and ZrCuAl MGs.

Although the medium-range NDG has a direct correlation with the SRO that may still dominate the cluster structures for the nearest neighboring atoms in both the ML and MG, there are important differences in nature between the NDG and the SRO. The viscosity of the ML increases very rapidly during the cooling process. As the temperature decreases to the glass-forming temperature, the viscosity of a supercooled ML will be many orders higher than that of an undercooled ML. It is clear that this rapid increase in viscosity is most likely due to the formation of an NDG in the supercooled ML. As a result, the temperature dependence of the NDG is obviously distinct from that of the SRO, and the transition from the ML to the MG is indeed triggered by the freezing of the NDG at the glass-forming temperature, rather than being due to the SRO.

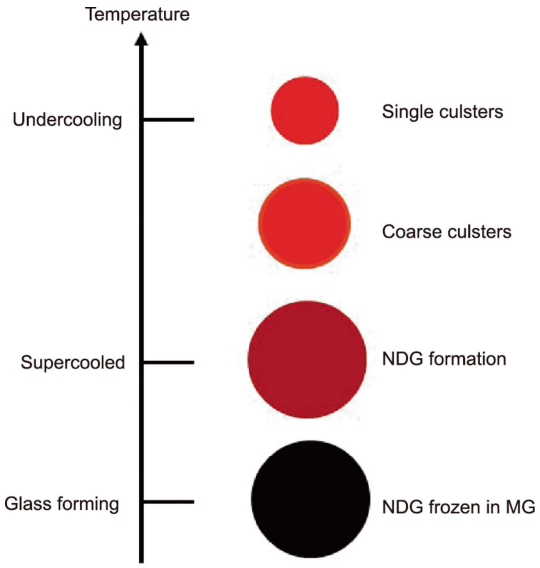

Fig. 7. Schematic illustration of microstructure development from an ML to an MG. Individual single clusters in the undercooling ML coarsen as the temperature decreases and an NDG is formed in the supercooled ML. Finally, the NDG freezes in the MG at the glass-forming temperature.

Furthermore, another important difference between the NDG and the SRO is that the environment-dependent energetic properties of the local cluster structures constructed by a medium-range NDG promote the structural stability of the MG and the supercooled ML, in addition to being responsible for a rapid increase in viscosity during the cooling of the ML and the initiation of the transition from the ML to MG.

Geometrically, for icosahedral packing, 12 atoms are positioned around a central atom to form 20 isometric triangles at the whole surface; together with the central atom, these 12 shell atoms further form 20 tetrahedrons. Thus, a single tetrahedron has nearly the same APD as the icosahedron and can also promote the glass-forming ability of the ML in the same way as the icosahedron. Therefore, a tetrahedron with a spatial scale of a few atoms is the smallest densely close-packed cluster for a density gradient in both MLs and MGs. As a result, in principle, the scale of the density gradient can range from a single tetrahedron to interconnected icosahedron-like clusters. The observed scale of the density gradient is also related to the effect of the cooling rate—that is, faster cooling rates usually depress cluster coarsening and produce a lower connectivity of atomic clusters, leading to smaller density motifs and/or clusters. Experimentally, at a cooling rate of approximately 10^6 $K{\cdot}s^{-1}$ for the transition from an ML to an MG, the coarsening and interconnection of the icosahedron-like clusters have been found to be limited to occurring between neighboring clusters only within a spatially critical nanoscale length [19,45]. In addition to the cooling rate effect, the coarsening and connectivity of the clusters are temperature dependent and local-structure dependent [42,45]. A difference in local structures may lead to dynamic heterogeneity in the glass-forming liquid, which corresponds to structural heterogeneity in the microscopic structure represented by the NDG accompanied by its varied spatial scale in the MG.

During the transition from an ML to an MG, morphological alternation of the coarse clusters due to their surface reconstruction is strongly dominated by the minimal total surface energy, which can be roughly determined by the product of the total surface area and the energy per unit of area. When the clusters merge together, the local or whole structure of the newly formed cluster can be changed if the atoms at the joint area rearrange in a different packing manner compared with that of the original clusters. Even if the rearrangement of the atoms at the joint area aligns with the packing manner of the original clusters, the surface morphology of the original cluster is maintained only if the specific number of atoms contained in the newly formed cluster construct a perfect outside shell.

Taking a coarse icosahedron as an example, it is known that the number of atoms required to construct the different perfect shells of an icosahedron must satisfy the $10n^2+2$ rule [46], where n is the number of the successive atomic shells. Therefore, this rule can easily be used to determine that there are 12 atoms in the first shell, and—if the coarse cluster still maintains perfect five-fold symmetrical vertices at the outside shells of the coarse icosahedron—there must be exactly 42 atoms in the second shell and 92 atoms in the third shell. The number of atoms in the outside shell of a coarse cluster is rarely exactly coincident to the specific number needed to maintain the perfect outside shell of the original clusters in the process of cluster coarsening. In most cases, instead of maintaining the perfect shell of the original clusters, the atoms are arranged in the outside shell of a coarse cluster in a manner that satisfies the minimal total surface energy, causing many different facets to be present on the outside surface. Therefore, the corresponding surface morphologies of the coarse clusters inevitably change completely or deviate from the original clusters to some extent. For example, instead of an imperfect icosahedron with incomplete pentagonal vertices at the outside shell, several

icosahedrons can shear one or several common atoms or inter-penetrate each other to form an icosahedral chain, similar to a connection of clusters, in order to maintain the minimal surface energy. Consequently, the structural evolution during the transition from an ML to an MG can result in coarse clusters and/or NDGs with different sizes and various surface morphologies.

5. Conclusions

We find that an NDG exists in the MGs and is closely correlated with the dominant icosahedron-like clusters with high APD in the MLs. During the transition from the ML to MG, the different clusters in the supercooled ML are rearranged according to descending APD order. Icosahedral and icosahedron-like clusters with high APDs are surrounded by non-icosahedral clusters with low APDs to form an NDG that stabilizes the supercooled ML state and remained in the MG. Depending on the NDG and the SRO, multi-scale characteristic structures can be well recognized in the MG. At the atomic and/or sub-nanometer level, the characteristic structure is dominated by the SRO, whereas the NDG dominates the characteristic structure at the nanometer and/or medium-range level. Furthermore, the random distribution of the NDG results in long-range disorder in the MG. Consequently, the NDG revealed in this study bridges the gap between SRO and long-range disorder and sheds new light on the nature of the microscopic structure inside MGs.

Acknowledgments

This work was supported by the National Natural Science Foundation of China (51971093, 52192603, and 51501043).

Compliance with ethics guidelines

Shaoxiong Zhou, Bangshao Dong, Yanguo Wang, Jingyu Qin, and Weihua Wang declare that they have no conflict of interest or financial conflicts to disclose.

Appendix A. Supplementary material

Supplementary material to this article can be found online at https://doi.org/10.1016/j.eng.2023.01.010.

References

[1] Ming X, Huang JC, Li ZJ. Materials-oriented integrated design and construction of structures in civil engineering—a review. Front Struct Civ Eng 2022;16(1):24–44.
[2] Cao CR, Huang KQ, Shi JA, Zheng DN, Wang WH, Gu L, et al. Liquid-like behaviours of metallic glassy nanoparticles at room temperature. Nat Commun 2019;10(1):1966.
[3] Sheng HW, Luo WK, Alamgir FM, Bai JM, Ma E. Atomic packing and short-to-medium-range order in metallic glasses. Nature 2006;439(7075):419–25.
[4] Elliott SR. Physics of amorphous materials. 2nd ed. Harlow: Longman Scientific & Technical; 1990.
[5] Kirkpatrick TR, Thirumalai D, Wolynes PG. Scaling concepts for the dynamics of viscous liquids near an ideal glassy state. Phys Rev A 1989;40(2):1045–54.
[6] Fan Z, Ding J, Ma E. Machine learning bridges local static structure with multiple properties in metallic glasses. Mater Today 2020;40:48–62.
[7] Xia X, Wolynes PG. Fragilities of liquids predicted from the random first order transition theory of glasses. Proc Natl Acad Sci USA 2000;97(7):2990–4.
[8] Liu XJ, Xu Y, Hui X, Lu ZP, Li F, Chen GL, et al. Metallic liquids and glasses: atomic order and global packing. Phys Rev Lett 2010;105(15):155501.
[9] Wu ZW, Li MZ, Wang WH, Liu KX. Hidden topological order and its correlation with glass-forming ability in metallic glasses. Nat Commun 2015;6(1):6035.
[10] Ding J, Patinet S, Falk ML, Cheng Y, Ma E. Soft spots and their structural signature in a metallic glass. Proc Natl Acad Sci USA 2014;111(39):14052–6.
[11] Bernal JD. Geometry of the structure of monatomic liquids. Nature 1960;185(4706):68–70.
[12] Miracle DB. A structural model for metallic glasses. Nat Mater 2004;3(10):697–702.
[13] Miracle DB. The efficient cluster packing model—an atomic structural model for metallic glasses. Acta Mater 2006;54(16):4317–36.
[14] Langer JS. Shear-transformation-zone theory of plastic deformation near the glass transition. Phys Rev E 2008;77(2):021502.
[15] Hirata A, Guan P, Fujita T, Hirotsu Y, Inoue A, Yavari AR, et al. Direct observation of local atomic order in a metallic glass. Nat Mater 2011;10(1):28–33.
[16] Angell CA. Formation of glasses from liquids and biopolymers. Science 1995;267(5206):1924–35.
[17] Debenedetti PG, Stillinger FH. Supercooled liquids and the glass transition. Nature 2001;410(6825):259–67.
[18] Hu YC, Li FX, Li MZ, Bai HY, Wang WH. Five-fold symmetry as indicator of dynamic arrest in metallic glass-forming liquids. Nat Commun 2015;6(1):8310.
[19] Liu XJ, Wang SD, Fan HY, Ye YF, Wang H, Wu Y, et al. Static atomic-scale structural heterogeneity and its effects on glass formation and dynamics of metallic glasses. Intermetallics 2018;101:133–43.
[20] Nelson DR. Order, frustration, and defects in liquids and glasses. Phys Rev B 1983;28(10):5515–35.
[21] Zhang P, Maldonis JJ, Liu Z, Schroers J, Voyles PM. Spatially heterogeneous dynamics in a metallic glass forming liquid imaged by electron correlation microscopy. Nat Commun 2018;9(1):1129.
[22] Lei TJ, DaCosta LR, Liu M, Wang WH, Sun YH, Greer AL, et al. Microscopic characterization of structural relaxation and cryogenic rejuvenation in metallic glasses. Acta Mater 2019;164:165–70.
[23] Pekin TC, Ding J, Gammer C, Ozdol B, Ophus C, Asta M, et al. Direct measurement of nanostructural change during *in situ* deformation of a bulk metallic glass. Nat Commun 2019;10(1):2445.
[24] Lu YM, Zeng JF, Wang S, Sun BA, Wang Q, Lu J, et al. Structural signature of plasticity unveiled by nano-scale viscoelastic contact in a metallic glass. Sci Rep 2016;6(1):29357.
[25] Lu BF, Kong LT, Laws KJ, Xu WQ, Jiang Z, Huang YY, et al. EXAFS and molecular dynamics simulation studies of Cu–Zr metallic glass: short-to-medium range order and glass forming ability. Mater Charact 2018;141:41–8.
[26] Huang B, Ge TP, Liu GL, Luan JH, He QF, Yuan QX, et al. Density fluctuations with fractal order in metallic glasses detected by synchrotron X-ray nano-computed tomography. Acta Mater 2018;155:69–79.
[27] Deo LP, Nikodemski S. Atom probe analysis of Ni–Nb–Zr metallic glasses. Bull Mater Sci 2020;43(1):44.
[28] Hosokawa S, Bérar JF, Boudet N, Pilgrim WC, Pusztai L, Hiroi S, et al. Detailed structural analysis of amorphous $Pd_{40}Cu_{40}P_{20}$: comparison with the metallic glass $Pd_{40}Ni_{40}P_{20}$ from the viewpoint of glass forming ability. J Non-Cryst Solids 2021;555:120536.
[29] Yavari AR. A new order for metallic glasses. Nature 2006;439(7075):405–6.
[30] Zeng Q, Sheng H, Ding Y, Wang L, Yang W, Jiang JZ, et al. Long-range topological order in metallic glass. Science 2011;332(6036):1404–6.
[31] Stevenson JD, Schmalian J, Wolynes PG. The shapes of cooperatively rearranging regions in glass-forming liquids. Nat Phys 2006;2(4):268–74.
[32] Yang Y, Zeng JF, Volland A, Blandin JJ, Gravier S, Liu CT. Fractal growth of the dense-packing phase in annealed metallic glass imaged by high-resolution atomic force microscopy. Acta Mater 2012;60(13–14):5260–72.
[33] Yang Y, Zhou J, Zhu F, Yuan Y, Chang DJ, Kim DS, et al. Determining the three-dimensional atomic structure of an amorphous solid. Nature 2021;592(7852):60–4.
[34] Ryu W, Yamada R, Saida J. Tailored hardening of ZrCuAl bulk metallic glass induced by 2D gradient rejuvenation. NPG Asia Mater 2020;12(1):52.
[35] Li X, Liu H, Cheng L. Symmetry-mismatch reconstruction of genomes and associated proteins within icosahedral viruses using cryo-EM. Biophys Rep 2016;2(1):25–32.
[36] Plimpton S. Fast parallel algorithms for short-range molecular dynamics. J Comput Phys 1995;117(1):1–19.
[37] Cheng YQ, Ma E, Sheng HW. Atomic level structure in multicomponent bulk metallic glass. Phys Rev Lett 2009;102(24):245501.
[38] Cowley JM. Diffraction physics. Amsterdam: North-Holland Publishing Corp.; 1975.
[39] Gellatly BJ, Finney JL. Characterisation of models of multicomponent amorphous metals: the radical alternative to the Voronoi polyhedron. J Non-Cryst Solids 1982;50(3):313–29.
[40] Miracle DB, Sanders WS, Senkov ON. The influence of efficient atomic packing on the constitution of metallic glasses. Philos Mag 2003;83(20):2409–28.
[41] Hao SG, Wang CZ, Li MZ, Napolitano RE, Ho KM. Dynamic arrest and glass formation induced by self-aggregation of icosahedral clusters in $Zr_{1-x}Cu_x$ alloys. Phys Rev B 2011;84(6):064203.
[42] Wong K, Krishnan RP, Chen C, Du Q, Yu D, Lu Z, et al. The role of local-geometrical-orders on the growth of dynamic-length-scales in glass-forming liquids. Sci Rep 2018;8(1):2025.
[43] Wu SQ, Wang CZ, Hao SG, Zhu ZZ, Ho KM. Energetics of local clusters in $Cu_{64.5}Zr_{35.5}$ metallic liquid and glass. Appl Phys Lett 2010;97(2):021901.
[44] Aliaga LCR, Lima LVPC, Domingues GMB, Bastos IN, Evangelakis GA. Experimental and molecular dynamics simulation study on the glass formation of Cu–Zr–Al alloys. Mater Res Express 2019;6(4)045202.
[45] Wei D, Yang J, Jiang MQ, Wei BC, Wang YJ, Dai LH. Revisiting the structure–property relationship of metallic glasses: common spatial correlation revealed as a hidden rule. Phys Rev B 2019;99(1):014115.
[46] Mackay AL. A dense non-crystallographic packing of equal spheres. Acta Cryst 1962;15(9):916–8.